THE ASTROPHYSICAL JOURNAL, 413:221–236, 1993 August 10

HIGH-RESOLUTION OBSERVATIONS OF TURBULENCE IN THE SUBCONDENSATION TMC-1C IN HEILES' CLOUD 2: ESTIMATION OF THE VELOCITY SPECTRUM OF TURBULENCE

Y. KITAMURA,[1] K. SUNADA,[2,3] M. HAYASHI,[2] AND T. HASEGAWA[4]

Received 1992 June 22; accepted 1993 February 19

ABSTRACT

We have made mapping observations of $4' \times 4'$ and $8' \times 8'$ areas of the subcondensation TMC-1C in Heiles' cloud 2 of the Taurus complex (140 pc) by using the 45 m telescope of Nobeyama Radio Observatory. The $^{13}CO(J = 1–0)$ and $C^{18}O(J = 1–0)$ lines were used and the beam size of the telescope was $\approx 17''$ (0.01 pc). From the raw data in each area we could extract fluctuating components whose wavelengths range from twice the grid spacing for our mapping to the size of our observed area, and the components are considered as turbulence in this study. We have evaluated unbiased autocorrelation functions (ACFs) of turbulent velocity and intensity fields from the ^{13}CO and $C^{18}O$ data, respectively, and the ACFs show meaningful correlations in the turbulent velocity and intensity fields. Based on the ACFs in the $4' \times 4'$ area we have estimated power spectra by a two-dimensional maximum entropy method. The velocity spectrum, equivalent to the lateral three-dimensional spectrum, does not decrease monotonically in proportion to the wavenumber, but increases in the range from 1/(0.05 pc) to 1/(0.03 pc), unlike Kolmogorov's 5/3 law. This feature indicates that the energy of the lateral part of turbulence per unit mass concentrates at the scales of $\lesssim 0.03$ pc, and that the energy dissipation does not occur at such small scales. Besides, the spectrum seems to have a peak at 0.15 pc, because turbulent motions having scales larger than ~ 0.15 pc are removed as ordered motions in our analysis.

Subject headings: ISM: individual (TMC) — ISM: kinematics and dynamics — ISM: molecules — turbulence

1. INTRODUCTION

The existence of turbulent gas motion in molecular clouds where new stars are born has been generally accepted from the observationally confirmed fact that various molecular lines have superthermal widths over a wide range of spatial scales. The widths of the lines are typically a few km s^{-1} in dark clouds and a few tens km s^{-1} in giant molecular clouds (GMCs). The thermal width, on the other hand, is 0.24 km s^{-1} with a typical cloud temperature of $T = 10$ K. The nonthermal broad widths can not be well explained by other processes like pressure broadening, Zeeman splitting, and so on. Taking account of the molecular viscosity, the Reynolds number is estimated to be of the order of 10^8 in molecular clouds, and such a large value is consistent with the turbulent state inside the clouds. Besides, the compressibility is dominant in the clouds because of the high Mach numbers of 10–100, and the turbulence as well as the gravitational instability complicates the density structure of the clouds. Actually, aperture synthesis observations of star-forming regions revealed very clumpy morphology down to a small scale of $\sim 1''$.

The studies of the turbulence in molecular clouds began with the pioneering work by Larson (1981). He derived the famous relation between the line width and the cloud size from the observational data of many clouds. The similarity between his relation and Kolmogorov's law has supported the scenario that the turbulence in molecular clouds with various scales was produced in the past owing to the energy cascade from the largest vortex that might be driven by the galactic differential rotation. Myers (1983) found a similar relation extended into the subsonic regime. However, no one can answer why Kolmogorov's law holds even in the case of the compressible interstellar medium. In addition to these size–line width relations, it has been shown that the energy of the turbulence is comparable with the gravitational energy (e.g., Larson 1981). The realization of the virial equilibrium is consistent with the following observational facts: The lifetime of molecular clouds is larger than their free-fall time, and the star formation rate in the clouds is much smaller than the predicted value by theoretical models of gravitationally collapsing clouds (e.g., see the review by Scalo 1985).

The recent development of radio telescope systems enables us to make efficient mapping with low noise over a vast area. Scalo (1984) tried to find a correlation length in the turbulent velocity field of a dense core in the ρ Oph cloud by a statistical method. He estimated the autocorrelation and structure functions of the velocity field. However, he could not find any correlation lengths, probably because the grid spacing of the $C^{18}O$ data he analyzed was coarse. After his work, Kleiner & Dickman (1987) analyzed the ^{13}CO data of Heiles' cloud 2. They found a correlation length of ~ 0.1 pc in the turbulent velocity field by evaluating the autocorrelation function, and showed that the energy dissipation rate of the turbulence has a single sharp peak at the length. They also suggested that the correlation length might determine the mass of new stars, because a region whose size is as large as the length contains $\sim 1\ M_\odot$, the typical mass of T Tauri stars. From another viewpoint, Falgarone (1989) and Falgarone & Phillips (1990) noted the wing components of line profiles with high signal-to-noise ratio, which were integrated over large mapping areas,

[1] Department of Liberal Arts, School of Allied Medical Sciences, Kagoshima University, Sakuragaoka 8-35-1, Kagoshima 890, Japan.
[2] Department of Astronomy, the University of Tokyo, Yayoi 2-11-16, Bunkyo-ku, Tokyo 113, Japan.
[3] Postal address: Nobeyama Radio Observatory, Nobeyama, Minamimaki-mura, Minamisaku-gun, Nagano 384-13, Japan.
[4] Institute of Astronomy, the University of Tokyo, Osawa 2-21-1, Mitaka, Tokyo 181, Japan.

and discussed that the components represent a signature of the intermittency that is considered as a fundamental property of turbulence.

Turbulence generally contains many vortices over a wide range of spatial scales. This feature hampers the understanding of turbulence by computer simulations. To simulate fully turbulent motions, many grid points with fine spacing are required, and calculations with such fine grids consume much time. Supercomputers recently developed, however, have a capability of performing some calculations of turbulence. Passot, Pouquet, & Woodward (1988) performed two-dimensional simulations of the turbulence in molecular clouds with Mach numbers close to unity. Although the compression of the gas is not dominant in flows with such low Mach numbers, it was shown that Kolmogorov-type spectra are compatible with the compressibility of the interstellar gas. They also pointed out the development of a highly filamentary structure in spite of no magnetic fields. Following this work, Léorat, Passot, & Pouquet (1990) investigated the influence of supersonic turbulence on gravitational collapse of clouds and showed that the cloud collapse depends on the ratio of the transfer time of compressible energy to the cloud free-fall time.

As described above, for understanding of the turbulence seen in molecular clouds, it is very important to obtain mapping data of the clouds with high angular and velocity resolutions over vast areas, or to make three-dimensional calculations including compressibility and self-gravity with many points on fine numerical grids by supercomputers. In this study we have observed the turbulence seen in TMC-1C by using the Nobeyama 45 m telescope with high sensitivity and with high angular and velocity resolutions, in order to reveal the detailed velocity and spatial structures of the turbulence in molecular clouds and to understand the influence of the turbulence on star formation. In the next section, the observed source TMC-1C and the observing techniques to obtain our data are described, and our statistical analysis of the turbulence in TMC-1C is shown in § 3. In § 4 we discuss the velocity and spatial structures of the turbulence. Our conclusions are summarized in the last section.

2. OBSERVATIONS

The object TMC-1C is one of the subcondensations in Heiles' cloud 2 of the Taurus complex. The complex is a nearby star-forming region, whose distance is estimated to be 140 pc (Elias 1978). This small value enables us to observe the region with high spatial resolution. In the complex, T Tauri stars having low masses of $\lesssim 1\ M_\odot$ are observed (Cohen & Kuhi 1979). Nevertheless, few signs of stars being formed at present are found, and no disruptive OB stars are seen. The large-scale structure of the complex is filamentary. Kleiner & Dickman (1985) found a velocity gradient across the minor axis of the filament, which may suggest a prolate structure. At smaller scales complicated cloud structures, which are partly due to hierarchical fragmentation and partly due to turbulence, are seen in the maps by radio telescopes. In the densest central part of the complex, Heiles' cloud 2, the extent of which is a few deg^2 in the sky plane, Schloerb & Snell (1984) discovered a rotating ring. The diameter of the ring is ~ 1.5 pc, the rotation velocity is ~ 1 km s^{-1}, and the ring is gravitationally fragmented into several subcondensations (see Fig. 1), whose masses are of the order of 10 $M_\odot$. They showed that the observed ring is consistent with numerical calculations for the ring formation during the collapse of a rotating cloud. The

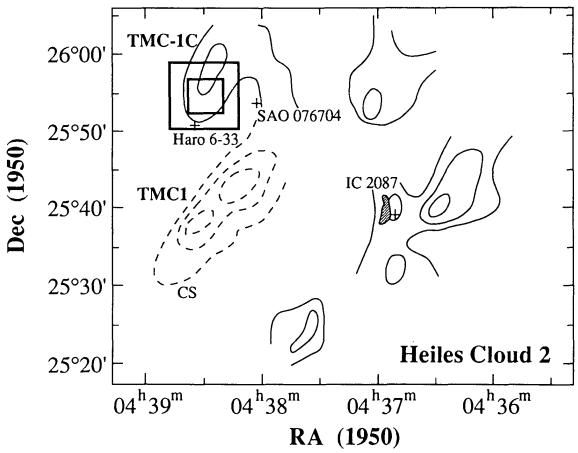

FIG. 1.—Our observed areas indicated by two squares at TMC-1C are superposed on the C^{18}O map of Heiles' cloud 2 by Schloerb & Snell (1984). The center position of the areas is at $(\alpha, \delta) = (4^h38^m30^s.0, 25°54'45''.0)$ (Schloerb & Snell 1984). The smaller 4′ × 4′ area was observed with a 20″ grid, and the larger 8′ × 8′ area with a 40″ grid. The number of grid points was 169 for both the two areas, and the beam size of the telescope was ≈17″.

subcondensation TMC-1C where we made our mapping is one of the high-density fragments in the ring. At the object, they reported that $T_R^*(C^{18}O) = 2.2$ K, $T_R^*(^{13}CO) = 5.2$ K, $\tau(^{13}CO) = 2.9$, and $M = 15\ M_\odot$.

Our observations were made in 1989 January and in 1991 April, using the 45 m telescope of Nobeyama Radio Observatory (NRO). We used the two ^{13}CO($J = 1$–0; 110.201 GHz) and C^{18}O($J = 1$–0; 109.782 GHz) lines. At 110 GHz the beam size was ∼17″ (0.012 pc), and the forward spillover and scattering efficiency η_{fss} was estimated to be ∼0.8 from the observation of the Moon. The two CO lines were simultaneously received by the 100 GHz band SSB Schottky-diode mixer receiver cooled at 20 K. For pointing observations we also used the 40 GHz band SSB Schottky-diode mixer receiver. A polarization diplexer was put in the quasi-optical system in the telescope to separate the two orthogonal polarizations. The single-sideband system noise temperatures including atmospheric, antenna, and transmission losses were typically 770 K for the ^{13}CO transition and 600 K for C^{18}O in 1989 January, and 700 K for ^{13}CO in 1991 April at the elevation of 70°. At the back end of the receivers we used a 2048 channel acousto-optical spectrometer (AOS) with a 20 kHz channel spacing. The frequency resolution was 37 kHz, corresponding to a velocity resolution of 0.1 km s^{-1} at 110 GHz.

We mapped a 4′ × 4′ (0.16 × 0.16 pc) area of TMC-1C by using the two CO lines in 1989 January. The map center was at $(\alpha[1950], \delta[1950]) = (4^h38^m30^s.0, 25°54'45''.0)$ (Schloerb & Snell 1984). The grid spacing was 20″ (0.014 pc) in both α and δ directions, which was nearly equal to the beam size. Therefore the main beam of the telescope could fully cover the mapping area as efficiently as possible, although it is the most desirable, from the sampling theorem, that the grid spacing be smaller than half of the beam size. The total number of the observed grid points was 169. In 1991 April we made another mapping observation over a larger 8′ × 8′ (0.33 × 0.33 pc) area with a grid spacing of 40″ (0.027 pc), using only the ^{13}CO transition. The map center was the same position as in the 4′ × 4′ area. In Figure 1, the two square areas observed by us are superposed on the C^{18}O map obtained by Schloerb & Snell (1984).

Pointing calibration was made at the interval of 2 hr by observing the SiO($v = 1$, $J = 1$–0) maser emission from NML-Tau ($\alpha[1950] = 3^h50^m43^s.6$, $\delta[1950] = 11°15'32''.0$), which is about 18° away from TMC-1C. The pointing error did not seriously affect our data, because we obtained the major part of the data when the wind velocity was less than 6 m s^{-1}. In such cases it is assured that the pointing error does not much exceed 5″.

By the chopper wheel calibration method, we derived the source antenna temperature T_A^*, which was corrected for atmospheric attenuation, ohmic losses, and rearward spillover and scattering. To obtain physical quantities of the cloud, we use the temperature T_R^* ($\equiv T_A^*/\eta_{fss}$), which corresponds to the source intensity convolved with the antenna diffraction and error patterns, instead of T_R ($\equiv T_R^*/\eta_c$), because we could not estimate the antenna–source coupling efficiency η_c. (For these definitions, see Kutner & Ulich 1981.) We employed a position-switching method and took the OFF position of ($\Delta\alpha$, $\Delta\delta$) = (35′, 35′), which was measured from the map center. All the data were taken at elevations higher than 30°, and during the mapping observations the reference spectra at the mapping center were monitored.

3. RESULTS

3.1. *Observed Data of the* ^{13}CO *and* C^{18}O *Lines*

For the 4′ × 4′ area mapped first, two velocity profiles of ^{13}CO($J = 1$–0) and C^{18}O($J = 1$–0) have been obtained at each grid point. The typical rms noise levels (i.e., 1 σ levels) induced by the telescope system are 0.30 and 0.23 K for ^{13}CO and C^{18}O, respectively. We show the two profiles averaged over the area in Figure 2*a*. The profile of ^{13}CO has a broad peak with a width (FWHM) of 0.95 km s^{-1} and has a subcomponent on the redshifted side. The profile of C^{18}O has a narrow single peak with a width of 0.49 km s^{-1}. The peak temperature of ^{13}CO is 4.0 K, which is smaller than the value of 5.2 K obtained by Schloerb & Snell (1984), while the peak temperature of C^{18}O is 2.7 K, which is a little larger than their value of 2.2 K. These disagreements are not problematical because our observed area does not overlap completely with their area for TMC-1C, as shown in Figure 1. The average velocities over the 4′ × 4′ area are 5.32 and 5.11 km s^{-1} for ^{13}CO and C^{18}O, respectively, compared with the value of 5.3 km s^{-1} obtained by Schloerb & Snell (1984). We also made observations of ^{13}CO in the larger 8′ × 8′ area containing the 4′ × 4′ area. The ^{13}CO profile averaged over the 8′ × 8′ area agrees well with the ^{13}CO profile shown in Figure 2*a*. The typical rms noise level is 0.29 K, and the average velocity is 5.15 km s^{-1}.

In Figure 2*b* the optical depths of the two lines are estimated from the ratio of the temperatures T_R^*, adopting the value of 0.18 (terrestrial value) as the C^{18}O to ^{13}CO abundance ratio. Here we assumed LTE conditions and used a common excitation temperature T_{ex}. It is valid to use the temperature T_R^* instead of T_R, if the two species have similar spatial distributions (i.e., similar coupling efficiencies η_c). It is found that the core component of ^{13}CO is optically thick, while the wing component is optically thin. The maximum value of the optical depth is 6.2 near the line center. This value is consistent with the evaluation of the ^{13}CO opacity at each grid point in our mapping area: For the ^{13}CO optical depth at the peak velocity of the C^{18}O emission, the maximum, mean, and minimum values are 19, 7, and 3 with a standard deviation of 3. On the contrary, the C^{18}O emission is approximately considered to be optically thin all over the velocity range. Therefore, the C^{18}O line may be more appropriate for the analysis of turbulence than the ^{13}CO line, although the wing emission of C^{18}O is very weak. If molecular clouds mainly consist of numerous small optically thick clumps, as suggested by Snell et al. (1984) for high-velocity molecular outflows, then we may be able to use the ^{13}CO data for the analysis of turbulence in spite of the large optical depth.

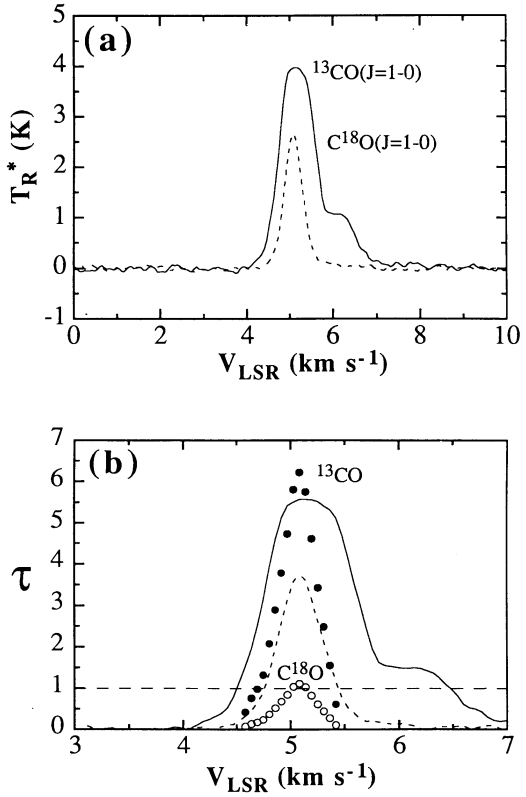

FIG. 2.—(*a*) Averaged profiles of the ^{13}CO($J = 1$–0) (*solid line*) and C^{18}O($J = 1$–0) (*broken line*) emission over the 4′ × 4′ area. (*b*) Optical depths of the two lines. Filled and open circles correspond to the optical depths of ^{13}CO and C^{18}O, respectively, at each velocity channel, and the averaged profiles of the two lines are also drawn.

Figure 3 shows the maps of the total integrated intensities of the ^{13}CO and C^{18}O emission in TMC-1C. A northwest-southeast gradient is seen in the two ^{13}CO maps. In addition, a clumpy structure is distinct, probably because the line traces the fluctuation of the surface temperature of the cloud owing to the large optical depth. On the other hand, the optically thin C^{18}O line traces a ridgelike structure from north to south, which has already been found in the large-scale C^{18}O map by Schloerb & Snell (1984) (see Fig. 1). The gradient seen in the ^{13}CO maps is consistent with this ridge, suggesting that the surface temperature of the ridge increases toward its central (i.e., northern) part. The CCS observations of TMC-1C by Yamamoto et al. (1993) revealed two peaks of a size of $\approx$0.04 pc inside the north-south ridge. The distance between the two peaks is about 0.15 pc. They also found a velocity gradient of $\approx$0.9 km s^{-1} pc^{-1} from SE to NW.

3.2. *Calculations of Centroid Velocities and Total Intensities*

We calculate the centroid velocities and total intensities from the velocity profiles of ^{13}CO and C^{18}O at each grid point.

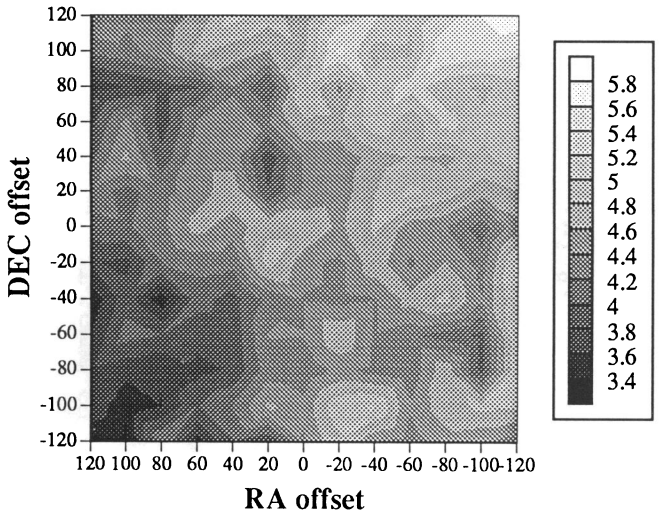

FIG. 3*a*

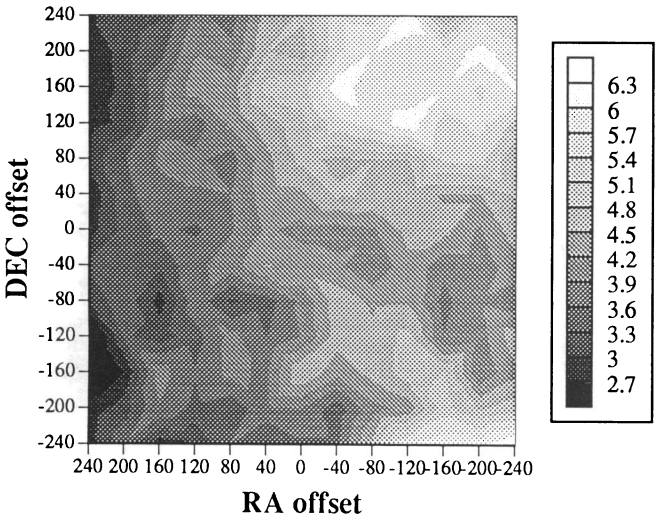

FIG. 3*b*

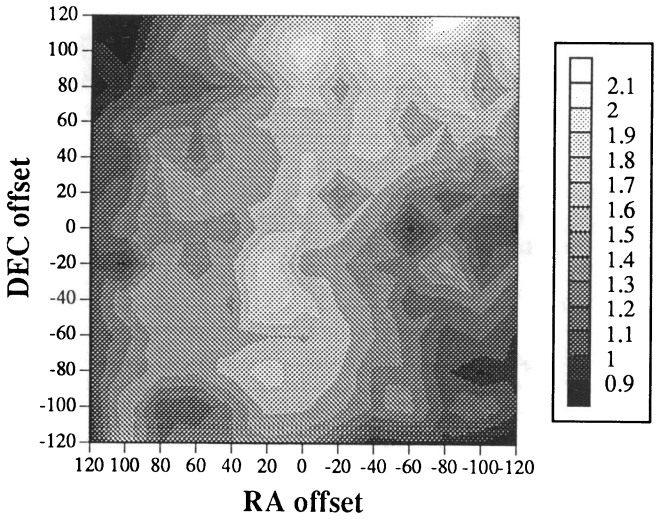

FIG. 3*c*

FIG. 3.—Total integrated intensity maps of ^{13}CO in the 4′ × 4′ area (*a*) and in the 8′ × 8′ area (*b*), and total intensity map of $C^{18}O$ in the 4′ × 4′ area (*c*). The levels of the gray scales in units of K km s^{-1} are written in the right elongated boxes. The offset values measured from the map center are in units of arcseconds.

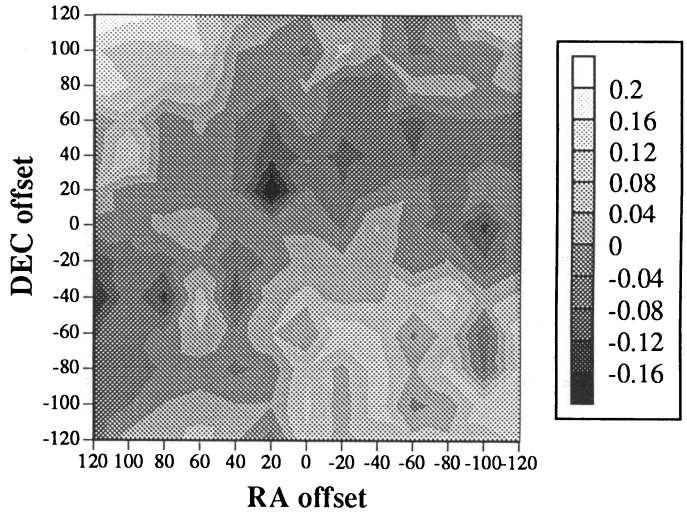

FIG. 4*a*

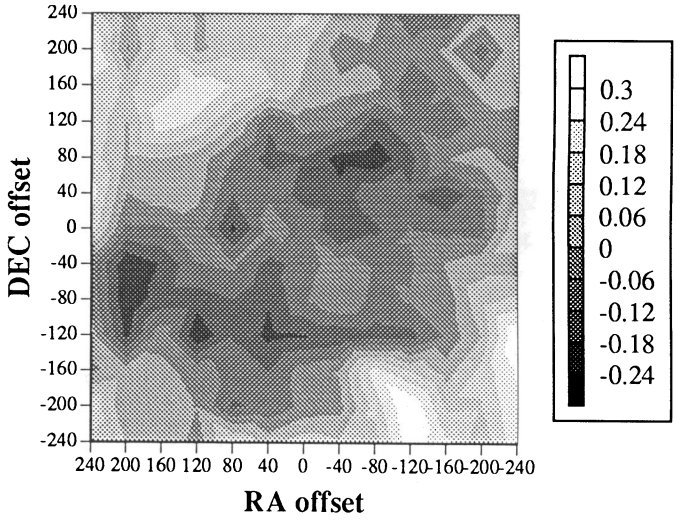

FIG. 4*b*

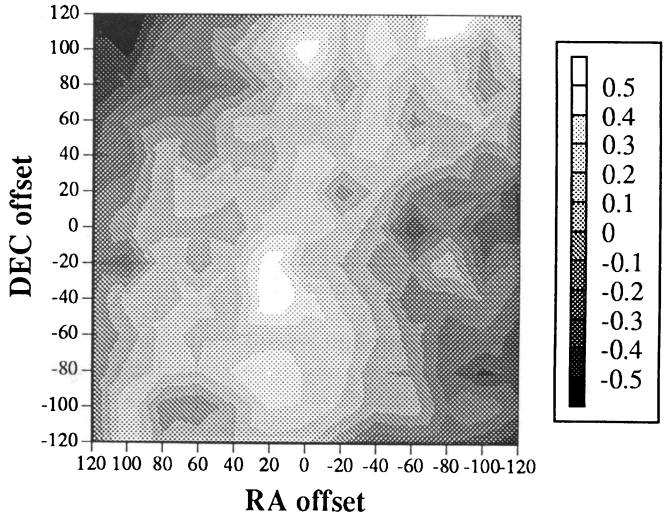

FIG. 4*c*

FIG. 4.—Contour maps of the turbulent velocity field of ^{13}CO in the 4′ × 4′ area (*a*) and in the 8′ × 8′ area (*b*), and contour map of the turbulent intensity field of $C^{18}O$ in the 4′ × 4′ area (*c*). The levels of the gray scales written in the right elongated boxes are in units of km s^{-1} for the velocity field and in units of K km s^{-1} for the intensity field. The offset values measured from the map center are in units of arcseconds.

The centroid velocity V_C (Dickman & Kleiner 1985) and total intensity I_T at the (i, j)th grid point are defined by

$$V_C(i, j) = \frac{\int_{v_1}^{v_2} vT_R^*(v; i, j)dv}{\int_{v_1}^{v_2} T_R^*(v; i, j)dv} \quad (1)$$

and

$$I_T(i, j) = \int_{v_1}^{v_2} T_R^*(v; i, j)dv , \quad (2)$$

where v means the radial velocity along the line of sight. For ^{13}CO, the mean of the centroid velocity is 5.32 km s^{-1}, its standard deviation is 0.07 km s^{-1}, and the rms noise level is 0.02 km s^{-1} in the 4′ × 4′ area. In the 8′ × 8′ area the mean, standard deviation, rms noise level are 5.16, 0.13, and 0.02 km s^{-1}, respectively. For the total intensity of C^{18}O, the mean is 1.34 K km s^{-1}, the standard deviation is 0.25 K km s^{-1}, and the rms noise level is 0.05 K km s^{-1}. The comparison between these standard deviations and rms noise levels suggests that autocorrelations will not be buried in the noise if the correlations truly exist.

To analyze statistically the turbulent velocity field, we subtract an average value V_0 from each centroid velocity calculated by equation (1). This is equivalent to replacing v in the integrand of the numerator of equation (1) by $v - V_0$. Consequently, it is found that the contribution of the wing emission to the integral of the numerator is large as compared with that of the core emission. This fact suggests that we can analyze the turbulence by using the ^{13}CO data in spite of the large optical depth at the line center, because the wing emission of ^{13}CO is shown to be optically thin. This possibility will be quantitatively confirmed in § 4.1. For the intensity field calculated by equation (2), on the other hand, we must use the data of the optically thin C^{18}O line instead of the ^{13}CO data, because the contribution of the core emission to the integral dominates that of the wing emission.

In calculating the centroid velocity and total intensity at each position, we used common values of v_1 and v_2 at all the observed positions for the first time. We tried to minimize the influence of the noise by changing the values of v_1 and v_2, and obtained more increased correlations with making the velocity range of the integration narrower. However, it is not physically clear which velocity range we should take. Therefore we abandon this method and introduce a threshold level to minimize the addition of the noise: We adopt only the data in the spectrometer channels whose intensities are above the threshold level, and discard the other channels. For the 1 σ threshold level, even the weak emission of the wing component can be picked up. However, about 16% of the channels containing only the noise are mistaken for channels containing a signal, and as a result, the noise propagated from the telescope system may seriously fluctuate the calculated V_C and I_T. For the 3 σ threshold level, on the other hand, only 0.15% of the noise is mistaken for a signal, and the noise will be considerably excluded. In this case, however, the major part of the weak wing component, which would mainly contribute to the calculations of V_C, will be excluded. Since the peak level of the noise is at about the 1.5 σ level, the threshold level of 2 σ seems to be the best choice. To examine practically the influence of the noise, we estimated autocorrelation functions (ACFs) for three cases of the 1 σ, 2 σ, and 3 σ threshold levels. The comparison among the three cases assures that the calculated ACFs do not sensitively depend on the adopted threshold level. Consequently, we adopt the 2 σ threshold level for our estimation of the centroid velocities and total intensities.

The calculations of the centroid velocities and total intensities by means of the above procedure were automatically done for each grid point by a computer. However, since the computer cannot exclude the spikelike noise that rarely exceeds our adopted threshold level, we needed to examine the validity of the channels selected by the computer for all the grid points.

3.3. *Separation of Turbulent and Ordered Components of the Velocity and Intensity Fields*

We tried to separate components of turbulent motions from components of systematic motions, on the basis of the spatial distributions of the calculated centroid velocities and total intensities. It is not easy to distinguish turbulent components from systematic ones in the small areas of the cloud we observed. This is because turbulent motions having spatial scales larger than the size of our observed areas come to be recognized as systematic motions. On the contrary, the data analyzed by Kleiner & Dickman (1987) covered the entire region of Heiles' cloud 2, and they could unambiguously separate turbulent components from systematic ones, the motion of the center of gravity and the rotation of the whole cloud. Ideally speaking, it is necessary to observe a whole cloud even for the analysis of turbulence in small subcondensations. Presently observations covering large areas with high angular resolutions are virtually impossible, and we do not have the data for the whole cloud. Thus we must look for the second-best method to analyze the turbulence seen in the small areas.

For our analysis, we adopted a simple procedure as follows: We considered constant (zeroth-order) and linear (first-order) components as systematic motions and removed these components from the data. Of course, the zeroth-order component corresponds not only to the motion of the center of gravity of the subcondensation TMC-1C, but also to some turbulent motions having spatial scales larger than the size of our observed areas. In addition, when the whole cloud of Taurus rotates around an axis (Kleiner & Dickman 1987), its rotation may produce a linear gradient inside the observed area much smaller than the Taurus complex. Therefore we should exclude the linear component from our data. It is possible that the linear component also includes some turbulent motions with spatial scales as large as the size of the observed areas. No distinct linear gradient is found in the velocity field of ^{13}CO and the intensity field of C^{18}O, which are used in our analysis of the turbulence in TMC-1C. Therefore, ambiguities concerning the subtraction of the linear component are excluded from our analysis. For the intensity field of ^{13}CO and the velocity field of C^{18}O, on the other hand, there exist northwest-southeast and southwest-northeast gradients, respectively.

In the above procedure, we can not extract large-scale disordered motions in our observed small areas and can analyze only some part of the turbulence in the cloud: The removal of the zeroth-order component from the data obtained by a Gaussian beam on a mapping grid is approximately equivalent to the usage of a filter transmitting only the signal whose wavenumber ranges from $1/D$ to $1/(2d)$, where D is the size of the observed area and d is the grid spacing, nearly equal to the beam size. Later, the behavior of estimated power spectra of the turbulence will confirm this interpretation. In our discussion we must have the incompleteness of our definition of turbulence in mind.

Figure 4 shows the contour maps of the ^{13}CO velocity and C^{18}O intensity fields of the turbulence, where the constant

components have been removed. The maps show some hierarchy from the size of the larger observed area (0.33 pc) down to the smaller grid spacing (0.014 pc), or the beam size of the telescope (0.012 pc). The hierarchy contains various scales, and the ACFs will pick up a typical scale among them. Therefore power spectra are more appropriate than the ACFs in order to describe these structures (e.g., Houlahan & Scalo 1990). The turbulent intensity map of $C^{18}O$ shows a ridgelike feature even after the removal of the zeroth-order component, and the velocity maps of ^{13}CO indicate some anticorrelation with the intensity map of $C^{18}O$. The velocity map of 4′ × 4′ area does not seem to agree with the inner part of the velocity map of 8′ × 8′ area; the disagreement is attributed to both the difference between the two grid spacings and the incompleteness of our definition of turbulence.

3.4. *Evaluation of Autocorrelation Functions of the Turbulence in TMC-1C*

Once the components of the turbulence are defined, we can easily estimate the autocorrelation functions (ACFs) of the turbulence by spatial average, according to the ergodic hypothesis. The ACF of the velocity field at the lag vector of (k, l) is calculated by

$$C(k, l) = \frac{\sum_{i,j} \delta V_C(i, j)\delta V_C(i + k, j + l)/N(k, l)}{\sum_{i,j} \delta V_C(i, j)\delta V_C(i, j)/N(0, 0)}, \quad (3)$$

where C is the ACF, δV_C indicates the turbulent component of the velocity field, and $N(k, l)$ is the number of data pairs at the (k, l) lag. A similar equation is applied to the turbulent component of the intensity field, δI_T. Note that the ACFs directly derived from the mapping data are the two-dimensional ones that are integrated along the line of sight and that are convolved with the beam pattern of the telescope, and not the true ACFs defined in the real three-dimensional space. According to the study by Dickman & Kleiner (1985), the true three-dimensional ACFs of the turbulence can be estimated from the two-dimensional ones obtained from radio data, when optically thin lines are used in observations. The correction for the influences of the beam pattern and the line-of-sight integration will be discussed in § 4. Hereafter we use the term "ACF" as the two-dimensional one and add the adjective "two-dimensional" if we must distinguish between the two- and three-dimensional ACFs.

Six ACFs of the turbulence in TMC-1C are shown in Figure 5. Except for the ACF of the ^{13}CO intensity field in the 4′ × 4′ area, all the ACFs show distinct positive correlations at small lags, although scatters of the correlations are seen. Only the profiles at the lags smaller than 0.1 and 0.2 pc are presented for the 4′ × 4′ and 8′ × 8′ areas, respectively, because statistical scatters considerably increase at large lags and absolute values of the ACFs even exceed unity. One of the physical quantities characterizing the ACFs is a correlation length, which is the spatial scale corresponding to the lag where the ACFs fall down to e^{-1}, following the definition by Kleiner & Dickman (1987). In the 4′ × 4′ area the ACFs of the velocity field show correlation lengths of ≈0.03 and 0.025 pc for the ^{13}CO and $C^{18}O$ lines, respectively. The ACF of the $C^{18}O$ intensity field shows a similar length of ≈0.04 pc, while the ACF of the ^{13}CO intensity field does not show any distinct length. In the 8′ × 8′ area, on the other hand, the ACFs show correlation lengths of ≈0.07 and 0.05 pc for the ^{13}CO velocity and intensity fields, respectively. The errors of the ACFs due to the noise propagated from the telescope system are estimated as Dickman & Kleiner (1985) did and are plotted by small bars in Figure 5.

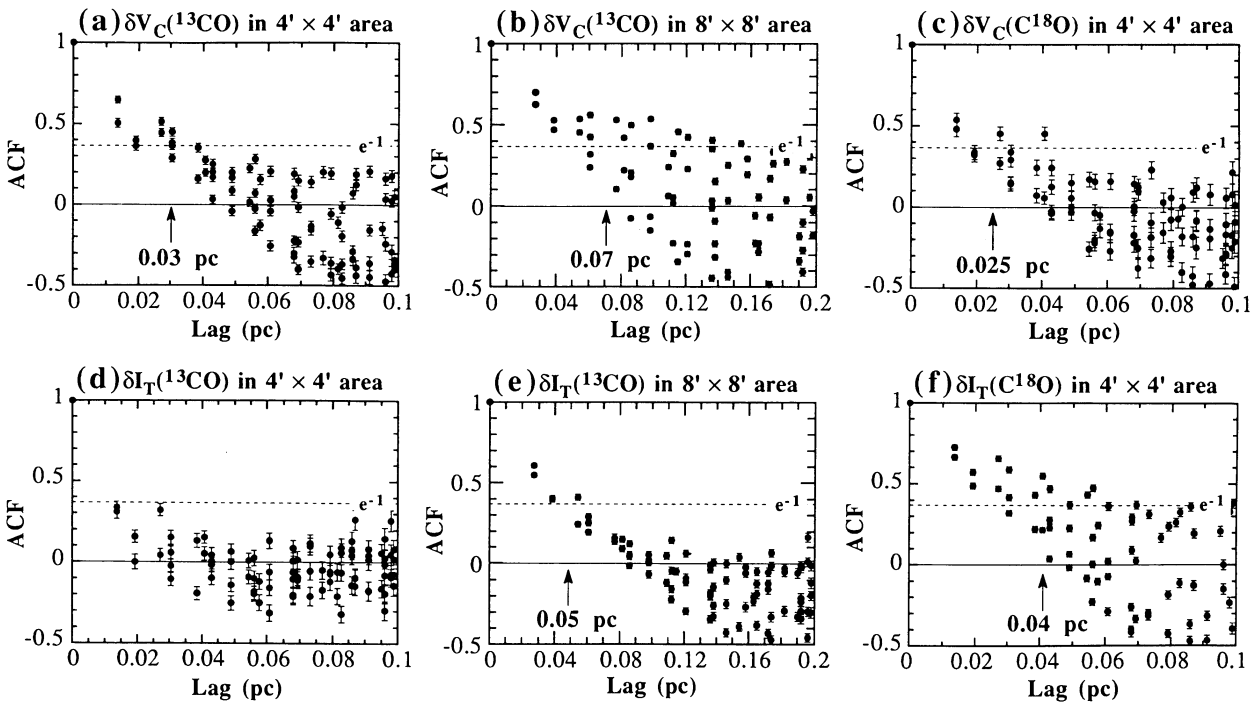

FIG. 5.—Six autocorrelation functions (ACFs) for the turbulent velocity (δV_C) and intensity (δI_T) fields of ^{13}CO and $C^{18}O$ in TMC-1C. The lag is in units of parsecs. For the 4′ × 4′ area, the ACFs at the lags smaller than 0.1 pc are shown, and for the 8′ × 8′ area the ACFs at the lags smaller than 0.2 pc are shown. In each panel the correlation length is designated by an arrow. The estimated errors are shown by small bars, and the levels of zero and e^{-1} are shown by solid and broken lines, respectively.

Figure 5 tells us that the influence of the noise on the ACFs is negligible, which has been already expected in § 3.2.

Kleiner & Dickman (1984) tried to replace the denominator $N(k, l)$ in equation (3) by $N(0, 0)$ or $[N(k, l)N(0, 0)]^{1/2}$ to reduce the statistical scatter at large lags. When we adopt $N(0, 0)$, the correlations at small lags may be seriously biased like $(D - r)/D$, where D is the size of the observed area and r is the absolute value of the lag vector. This is because the sizes of our observed areas are not sufficiently large compared with the correlation lengths. Therefore we adopt the unbiased estimator with the denominator of $N(k, l)$. Dickman & Kleiner (1985) pointed out that the magnitude of the correlations is reduced owing to the noise induced by the telescope system. The correlation at zero lag is the sum of the variance of the noise-free velocity fluctuation, σ_c^2 and the variance of the noise, σ_n^2, although the correlations at nonzero lags are not influenced by the noise. Consequently the ACFs including the noise are reduced by a factor of $[1 + (\sigma_n/\sigma_c)^2]^{-1}$. We made a correction by multiplying our estimated ACFs at nonzero lags by a factor of $1 + (\sigma_n/\sigma_c)^2$. The correlations at small lags slightly increased by this correction, because the factor is at most 1.1 in our data. After this correction we cannot find any factors biasing the ACFs at lower orders.

When we consider the ACFs as a function of the magnitude of the lag vector, the scatters of the plotted points are attributed to both the statistical scatter and the anisotropy of the turbulence, while the errors due to the noise propagated from the telescope system are estimated to be small as shown in Figure 5. The statistical scatter of the ACFs becomes large with increasing lag and fluctuates the estimated correlations around the true values to some extent. If the number of the data points is sufficiently large, the statistical scatter is reduced, and only the anisotropy remains. In this study, however, we cannot discriminate between these two kinds of scatters, and we sacrifice the anisotropy to reduce the statistical scatter as possible; the ACFs are averaged over the angular direction of the lag vector assuming isotropy, as was done by Scalo (1984). The profiles of the *isotropic* ACFs in Figure 6 show a slightly jagged feature at small lags, and this fact suggests that both the statistical scatter and the anisotropy would not seriously influence our discussion of spherically symmetric properties of the turbulence. Of course, the correlation lengths defined by the ACFs in Figure 5 agree with those by the *isotropic* ACFs in Figure 6.

3.5. *Evaluation of Structure Functions of the Turbulence in TMC-1C*

Another useful statistical measure to analyze turbulence is a structure function (SF). The structure function, S, at the (k, l) lag is defined by

$$S(k, l) = \frac{\sum_{i,j} \{\delta V_C(i, j) - \delta V_C(i + k, j + l)\}^2 / N(k, l)}{\sum_{i,j} \delta V_C(i, j)\delta V_C(i, j)/N(0, 0)} . \quad (4)$$

For globally homogeneous turbulence the ACFs are useful. However, such situations are not realistic in molecular clouds, and a more realistic approximation is local homogeneity, in which case the probability mean values of physical quantities of turbulent fields increase in proportion to spatial coordinates. In such cases the SFs are known to be appropriate, rather than the ACFs. For the globally homogeneous fields, the SFs come to be related with the ACFs as the following relation:

$$S(r) = 2[1 - C(r)] . \quad (5)$$

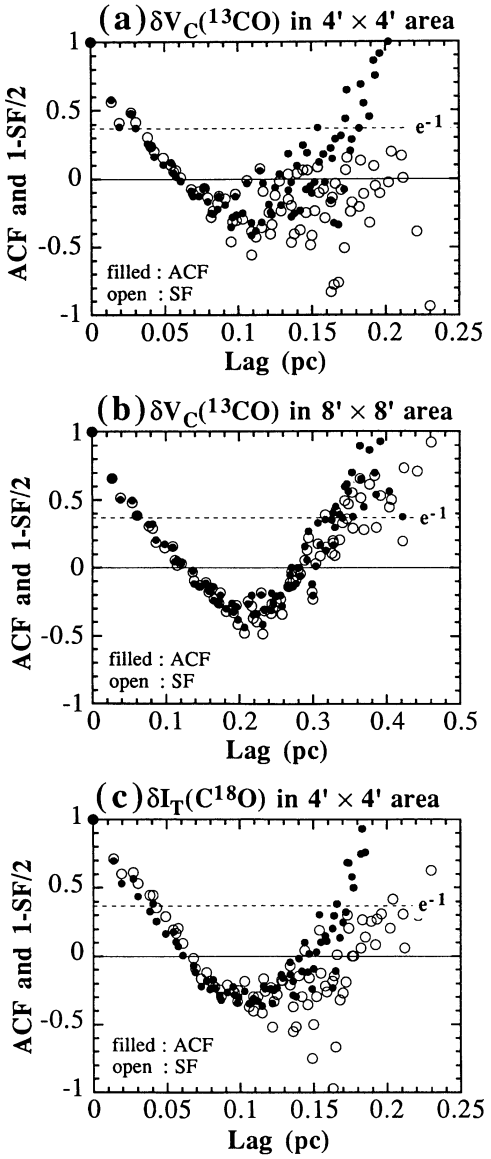

FIG. 6.—Isotropic autocorrelation functions (ACFs) plotted by filled circles and isotropic structure functions (SFs) plotted by open circles for the turbulent ^{13}CO velocity (δV_C) and $C^{18}O$ intensity (δI_T) fields. Instead of the SFs themselves, we show the functions of $1 - SF/2$ for the comparison with the ACFs. The profiles of the ACFs and SFs are averaged over the angular direction of the lag vector assuming spherical symmetry. The lag is in units of parsecs and the profiles all over the lag ranges are shown. The levels of zero and e^{-1} are shown by solid and broken lines, respectively.

The SF becomes proportional to $r^{2/3}$ for the Kolmogorov-like turbulence, and the function is convenient for the analysis of relations between velocity dispersions and spatial scales. Scalo (1984) used the SF to analyze the turbulence in the ρ Oph cloud, and O'Dell & Castañeda (1987) used the function for the turbulence seen in H II regions.

We calculated the SFs of the turbulent velocity and intensity fields in TMC-1C. The estimated SFs are shown in Figure 6. These SFs are averaged over the angular direction of the lag vector as well as the ACFs, and we display $1 - S(r)/2$ instead of $S(r)$ itself for the comparison with the ACFs. At the lags smaller than $\sim$0.1 pc, the isotropic SFs do not seriously differ from the

isotropic ACFs, and at larger lags the SFs tend to show smaller correlations than those by the ACFs. Because of the good agreement between the two functions at the lags smaller than 0.1 pc, we discuss the turbulence in TMC-1C by means of the ACFs.

3.6. *Estimation of Velocity and Intensity Power Spectra of the Turbulence in TMC-1C*

We have estimated power spectra consistent with the *isotropic* ACFs that were calculated from our observed data in the 4′ × 4′ area, by employing a two-dimensional maximum entropy method (MEM). Figures 7*a* and 7*b* show the two-dimensional power spectra of the turbulent velocity and intensity fields, which are corrected for the beam pattern of the telescope. Later the velocity spectrum will be shown to be equivalent to *the lateral three-dimensional spectrum* F_{NN} *of turbulence* in our discussion. The broken lines show the estimated level of the noise induced by the telescope system. Furthermore, we get the spherically symmetric spectra by multiplying the corresponding two-dimensional ones by a factor of $4\pi k^2$, where k means the vector of the wavenumber. Here we assume that the turbulence is homogeneous and isotropic and that the observed lines are optically thin. These spectra are shown in Figures 7*c* and 7*d*. In contrast with the 4′ × 4′ area where a full sampling was made, only an undersampling was done for the 8′ × 8′ area, and power spectra are not estimated for the larger area.

It is clear from Figures 7*a* and 7*b* that the estimated power spectra of the velocity and intensity fields of the turbulence do not obey the power law with a single index like Kolmogorov's law. One peak is seen at the spatial scale of ~0.15 pc. From 0.15 to 0.05 pc, the spectra decrease and come to increase from 0.05 to 0.027 pc. According to the sampling theorem, we can not estimate the power spectra at the scales smaller than 0.027 pc, or twice the grid spacing. Although the estimated error tends to increase with decreasing the spatial scale (i.e., with increasing the wavenumber), the error is roughly one order of magnitude smaller than the power spectra. Therefore, the profiles of the power spectra profiles cannot be explained by the sum of Kolmogorov-like spectra and the noise spectra, and the increase found at the scales smaller than ~0.05 pc must be explained by some physical processes.

It is well known that the ACFs can be converted into power spectra by the Fourier transformation. Compared with the ACFs, the power spectra are more useful to study physical properties of turbulence. However, it is difficult to calculate the power spectra from the estimated ACFs, because the statistical scatter becomes larger with increasing the lag, and because the correlation cannot be estimated at a large number of points in a lag space. An FFT-technique is not a powerful tool when statistical scatters are large because of a small number of sampling grid points. In such cases an MEM is known to be an effective method. Although the MEM generally consumes much computational time, it can estimate the power spectra,

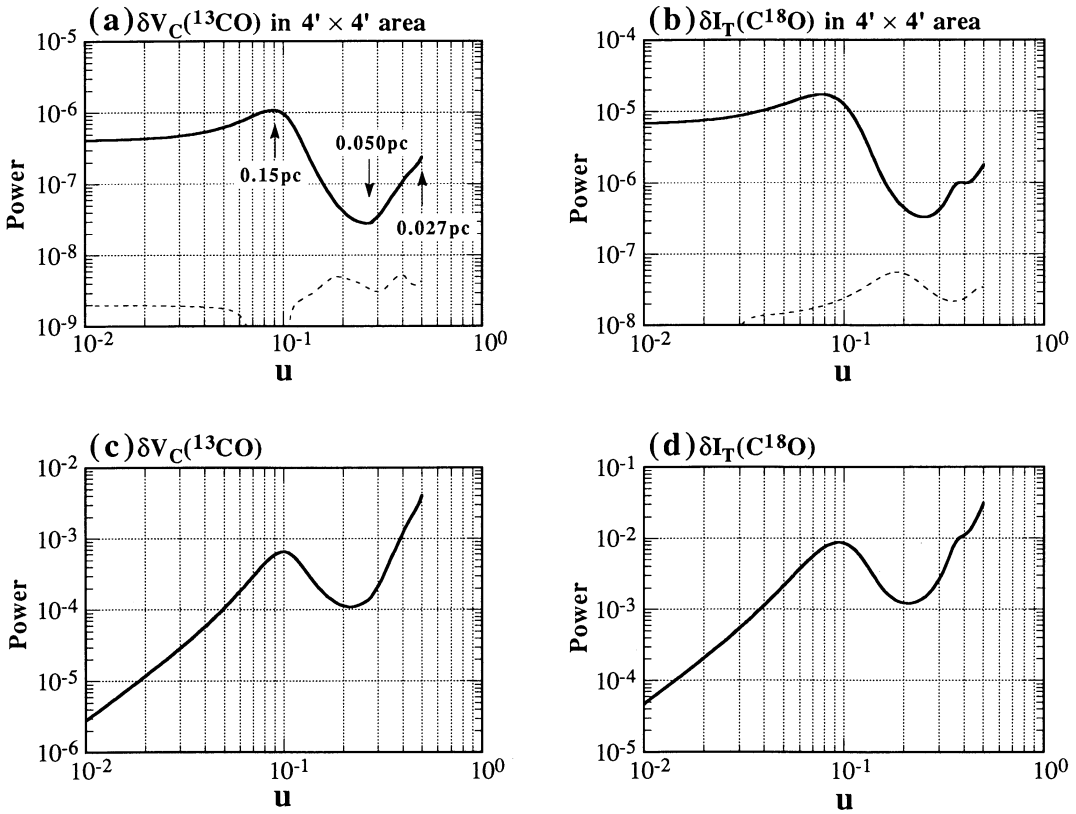

FIG. 7.—Estimated two-dimensional power spectra of the turbulent ^{13}CO velocity field (*a*) and $C^{18}O$ intensity field (*b*) in the 4′ × 4′ area. The velocity spectrum is equivalent to the lateral three-dimensional spectrum F_{NN} of turbulence. (*c*) and (*d*): Spherically symmetric spectra converted from the corresponding two-dimensional ones in the upper panels by multiplying a factor of $4\pi k^2$. The powers are in units of km^2 s^{-2} pc^3, K^2 km^2 s^{-2} pc^3, km^2 s^{-2} pc, and K^2 km^2 s^{-2} pc for (*a*), (*b*), (*c*), and (*d*), respectively, and in the abscissa we use the quantity $u = kd$, where d is the grid spacing, instead of the wavenumber k itself. In panel (*a*), three corresponding spatial scales are written in units of parsecs. Broken lines in the two upper panels show the noise levels. These spectra are calculated from the 9 × 9 correlation array using the truncated power series of the degree 39.

with some confidence, even from noisy data obtained with a small number of sampling points.

We used the convolution power algorithm proposed by Woods (1976). In this algorithm a maximum entropy spectrum is expanded into a power series and, as a result, the corresponding correlation function can be expressed by a convolution power (CP) series. If we find coefficients of the CP series so as to reproduce the observed ACF, then the maximum entropy spectrum will be obtained. The appropriate values of the coefficients are iteratively searched by using a gradient algorithm. If we truncate the CP series at a certain number of terms, an iteration equation becomes simple and faster convergence can be attained. However, we have no criteria for the degree M of the truncated series. By our numerical experiments 39 is an appropriate value for M. Even if we take larger values for M, the resulting spectra are not changed, but only the computational time lengthens. The convergence of the original algorithm is not very efficient, because approximate gradient forms were used. By using accurate gradient forms, we improved the original iteration scheme and obtained faster convergence. A remaining problem is how to determine the size of the correlation array where we try to fit a maximum entropy model to the ACFs. We tried spectral estimation for 3×3, 5×5, 7×7, ... and 13×13 arrays of nearest neighbors. For larger arrays, the profiles of the spectra become more jagged, although more information is incorporated. We obtained the best output for a 9×9 array, the size of which corresponds to the maximum lag of 0.08 pc. This is consistent with the fact that the profiles of the ACFs are smooth at the lags smaller than 0.1 pc and is consistent with the good agreement between the ACFs and SFs at the small lags. We examined our CP scheme for the two types of correlation functions, exponential and Gaussian ones, whose Fourier transformations are simple and analytic. It is confirmed that the CP scheme can reproduce the analytic spectral functions from the correlation data on 3×3, 5×5, 7×7, ... and 13×13 arrays. Ong (1971) proposed a gradient algorithm not by expanding a spectrum into a power series, but by integrating an accurate functional form. Although this method is more accurate than the CP method, it requires laborious computations because two-dimensional integration is needed at each iteration. We could get the convergence of Ong's iteration only for the three 3×3, 5×5, and 7×7 arrays, and the results agreed well with those obtained by the CP method. This agreement also supports the validity of our spectral estimation by the CP method.

If the correlation data on an array of nearest neighbors are given, we can directly estimate two-dimensional spectra, which are convolved with the Gaussian beam pattern of a radio telescope. In addition, the estimated spectra are the ones that passed through a filter. Roughly speaking, the filter can pass the signal whose wavelength ranges from $2d$ to D, where d and D mean the grid spacing and the size of the observed area. In our observations, the grid spacing is nearly equal to the beam size (HPBW) of the telescope, Θ. Although the signal filtered out cannot be recovered, it is easy to get rid of the influence of the Gaussian beam. The convolution with the beam pattern becomes an exponential factor in a wavenumber space as shown by equation (B5), and we can easily estimate the two-dimensional spectrum $F_2(\boldsymbol{k}_2)$ that is not convolved with the beam pattern of a telescope, from the spectrum $F_{\rm obs}(\boldsymbol{k}_2)$ directly estimated from the observed data. Since the exponential factor in equation (B5) becomes smaller than 0.17 for $|\boldsymbol{k}_2| > 1/(2d)$, the factor works as a filter cutting off the components having the wavenumbers larger than $1/(2d)$, and it is assured that the estimated spectra are not seriously influenced by the aliasing. We examined the influence of the aliasing for Gaussian and exponential spectra and for spectra obeying a power law with indices of -1 to -4, and concluded that the spectra were slightly raised only at the wavenumbers from $1/(2.5d)$ to $1/(2d)$. Therefore the increase at $kd = 0.3 \sim 0.5$ shown in Figure 7 cannot be produced by the aliasing.

4. DISCUSSION

4.1. *The Structure of the Turbulent Velocity Field in TMC-1C*

From the analysis by the ACFs, it is revealed that there exist at least three correlation lengths in the turbulent velocity field of Heiles' cloud 2. In the $4' \times 4'$ (0.16×0.16 pc) area the ACF of the ^{13}CO line shows a correlation length of $\sim$0.03 pc, and the ACF of C^{18}O shows a similar length of $\sim$0.025 pc. The fields of ^{13}CO and C^{18}O have a similar correlation length despite the difference between the optical depths of the two lines; the ^{13}CO line is optically thick for the core component and thin for the wing component, while the C^{18}O line is optically thin over the whole profile. This is because the wing component mainly contributes to the ACFs of the velocity field, as pointed out in § 3.2. To examine this interpretation, we obtained the turbulent velocity field by extracting the optically thin part of $V_{\rm LSR} \leq 4.7$ km s^{-1} and $V_{\rm LSR} \geq 5.4$ km s^{-1} (see Fig. 2*b*) from the ^{13}CO velocity profile at each grid point and estimated the velocity ACF. The resultant ACF for the optically thin part agrees with the ACF for all the velocity range, although the correlation slightly decreases. Consequently, it is confirmed that the turbulent velocity field can be analyzed from the ^{13}CO wing component as well as from the C^{18}O whole profile. In the $8' \times 8'$ (0.33×0.33 pc) area containing the $4' \times 4'$ one, the ACF of ^{13}CO shows a correlation length of $\sim$0.07 pc. Besides, in the $\sim 1^\circ \times 1^\circ$ (2.4×2.4 pc) area covering the inner region of Heiles' cloud 2, Kleiner & Dickman (1987) found a correlation length of $\sim$0.1 pc from the ACF of ^{13}CO. From the C^{18}O data, the masses of spheres whose radii are equal to the correlation lengths can be estimated to be 0.3, 1.6, and 3.2 $M_\odot$ for the lengths of 0.03, 0.07, and 0.1 pc, respectively.

A simple interpretation of the above facts is that the turbulence prevailing in Heiles' cloud 2 has hierarchical structure and that the hierarchy contains at least three discrete levels corresponding to the correlation lengths shown by the ACFs, unlike Kolmogorov's scenario. This interpretation is satisfactory if the medium scale of 0.07 pc does not exist. Since the size of the $4' \times 4'$ area is comparable with the scale of 0.1 pc found by Kleiner & Dickman (1987), we cannot recognize their scale, and we find a new small scale of 0.03 pc. Kleiner & Dickman (1987) could not find the scale of 0.03 pc from the data observed by Schloerb & Snell (1984), because the beam size of the telescope used by them was 53″ (0.036 pc). Even if the beam size is smaller than 0.03 pc, the typical turbulent motion in the small condensation TMC-1C will be buried under the motions with larger scales in Heiles' cloud 2. In fact, the ACF in the $4' \times 4'$ area becomes almost unity all over the lag range if we redefine the components of the turbulence by subtracting the velocity of 5.96 km s^{-1}, which is the mean velocity in Heiles' cloud 2 (Kleiner & Dickman 1987), from the centroid velocities estimated in TMC-1C. In such an ACF we cannot recognize the existence of the small scale of 0.03 pc. From the above discussion the coexistence of the two correlation lengths of 0.03

and 0.1 pc is consistent with the hierarchy model containing several discrete scales. However, the existence of the 0.07 pc scale does not seem to agree with the model. In the 8′ × 8′ area it is natural that we could not find the scale of 0.03 pc because of the 40″ (0.03 pc) grid. On the contrary it is unnatural that we found the scale of 0.07 pc instead of the scale of 0.1 pc, since the size of the 8′ × 8′ area is larger than the 0.1 pc scale. Is the difference between the scales of 0.07 and 0.1 pc due to the difference between the two observed areas? If the 0.07 pc scale truly exists, why could we not find the scale of 0.07 pc instead of the 0.03 pc scale in the 4′ × 4′ area whose size is about twice larger than 0.07 pc?

As discussed above, it seems to be unreasonable to consider that the correlation lengths shown by the ACFs in the small areas represent true physical scales characterizing the turbulence. This is mainly because we have no reliable method to separate turbulent components from systematic ones in the small areas observed by us, as previously stated; we cannot distinguish large-scale turbulent motions from systematic motions so far as the analysis is limited in a small area compared with the whole cloud. In contrast with our work, Kleiner & Dickman (1987) could truly get rid of systematic motions, because they analyzed the data obtained over the whole cloud. Therefore, we should take an interpretation that the correlation lengths derived by us do not directly reflect real physical scales in the cloud, and that the lengths reflect only the apparent typical scales seen in the gas motions that can be picked up as turbulence by individual observations made over the two areas. In fact, the correlation length seems to increase continuously with increasing the size of the analyzed area where the ACF is estimated, as shown in Figure 8. This relation can be considered as follows: The upper limit of the spatial scales of the turbulent gas motions that can be picked up in our analysis increases in proportion to the size of the analyzed area. If the gas motions with larger scales are taken into account, then the correlation length defined by the ACF lengthens. This interpretation will be validated from the analysis of the velocity power spectrum in § 4.3. Consequently, our derived scales from the ACFs are not true correlation lengths seen in the turbulence for lack of a reliable method to extract all the turbulent components in a limited small area. However, the correlation lengths derived in the small areas are useful to characterize the degree of correlations in the ACFs. Besides, our estimated ACFs do not lose their worth, because the profiles of the ACFs are closely related to power spectra of some components of the turbulence.

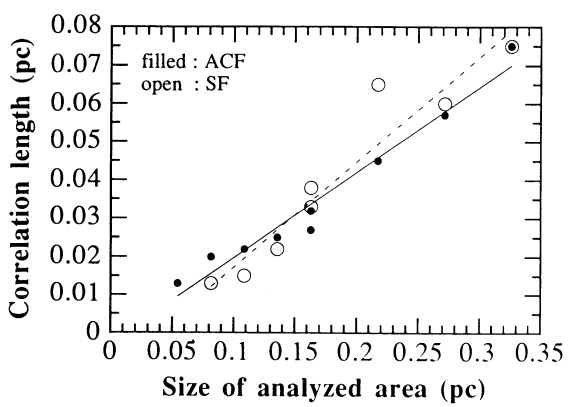

FIG. 8.—Relation between the correlation length (y) and the size of the analyzed area (x) for the ^{13}CO velocity field. The abscissa and ordinate are in units of parsecs. Filled and open circles correspond to the correlation lengths derived from the ACFs and SFs, respectively. The straight lines fitted to the data are $y = -0.002 + 0.22x$ (*solid line*) for the ACFs, and $y = -0.010 + 0.27x$ (*broken line*) for the SFs.

The correlations shown by the two-dimensional ACFs increase, compared with those shown by the three-dimensional ACFs, owing to the two following factors: the convolution with the beam pattern of a radio telescope and the integration along the line of sight. The ACFs do show a correlation length as large as the beam size of a telescope, even if the turbulence does not have any scales. Actually, even for white noise the ACF shows a correlation length of 0.85Θ, where Θ is the beam size (see eq. [A3]). Furthermore, when the three-dimensional ACF has a Gaussian form with a correlation length l_c, the apparent correlation length defined by the two-dimensional ACF becomes $(l_c^2 + \Theta^2/\ln 4)^{1/2}$ (see eq. [A6]). Therefore, correlation lengths comparable with the beam size are not true, but artificial. Since the ACF of the turbulent intensity field of ^{13}CO shows a correlation length of ~ 0.01 pc as small as the beam size (see Fig. 5*d*), it is found that the scale is artificial and the ACF shows no significant correlations. In addition to the convolution with the beam pattern, the correlations increase owing to the integration along the line of sight. For example, Kleiner & Dickman (1985) showed that the correlation lengths become twice as large as true scales in clouds at the worst. Taking account of the two influences, we derived the relation between the two- and three-dimensional ACFs as shown by equation (A5).

In the case of the velocity field, the correlation function $B[(\Theta^2u^2 + L^2x^2)^{1/2}]$ in equation (A5) must be expressed by two scalar functions even for the homogeneous and isotropic turbulence, because the velocity field is described by the two independent potential and solenoidal fields (Monin & Yaglom 1977). For simplicity of analysis we assume that the compressibility is not dominant in TMC-1C and that the velocity field can be described only by the solenoidal field, although the velocity widths (FWHM) of the ^{13}CO and C^{18}O lines exceed the sonic velocity. For the solenoidal velocity field $B[(\Theta^2u^2 + L^2x^2)^{1/2}]$ is replaced by $B_{zz}(\Theta u, Lx)$ of equation (B1), and B_{zz} is expressed by the function B_{LL} according to equation (B2). To the two-dimensional velocity ACF of ^{13}CO we fitted the following three models for $B_{LL}(r)$: (1) a Gaussian type of correlation function, $\exp[-(r/l_c)^2]$, where l_c means a correlation length; (2) an exponential type of correlation function, $\exp(-r/l_c)$; and (3) a Kolmogorov type of correlation function, $1 - 0.63(r/l_c)^{2/3}$. The Gaussian and exponential functions are proved to be correlation functions of some turbulence, and the Kolmogorov-type function is an approximate form. The power spectra of the Gaussian and exponential types have a single peak at the wavenumber corresponding to the correlation length l_c, and the spectrum of the Kolmogorov type has two scales corresponding to the energy injection scale, which is about twice as large as l_c (see eq. [25] of Kleiner & Dickman 1985), and the energy dissipation scale that is much smaller than l_c. The fitting results are shown in Figure 9a. The fitting does not seem to be good. The exponential type is the best, and the Kolmogorov type is the worst. The fitted values of the correlation length l_c are written in the figure. To get better fitting, steep and gentle gradients are required at small and large lags, respectively. This may require more complicated correlation functions, or the incorporation of both the solenoidal and potential components. For the cloud depth L we took three values of 0.16 pc (a typical size of the sub-

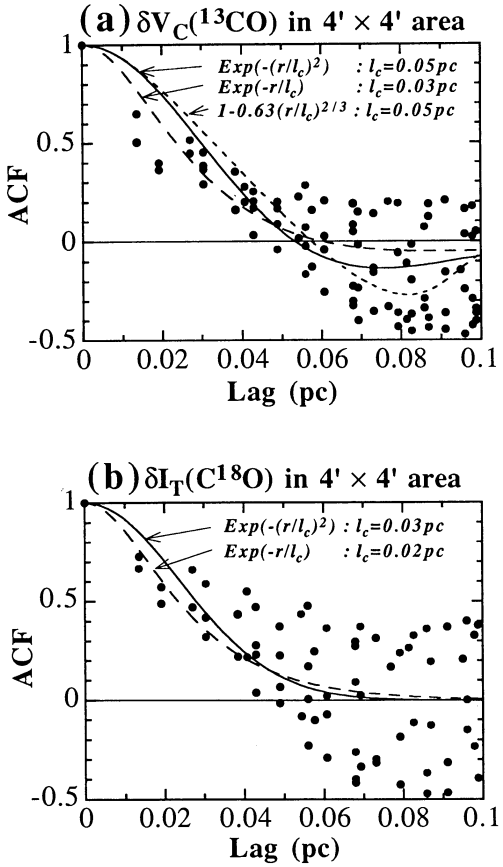

FIG. 9.—Three or two analytical functions fitted to the ACFs of the turbulent ^{13}CO velocity field (*a*) and $C^{18}O$ intensity field (*b*) in the 4′ × 4′ area; Gaussian, exponential, and Kolmogorov-type functions. The fitted values of the correlation length l_c are drawn in each panel.

condensations in Heiles' cloud 2), 1.2 pc (the size of Heiles' cloud 2), and 2.4 pc (a typical width of the Taurus filament). The fitting results did not depend on the cloud depth *L*.

4.2. *The Structure of the Turbulent Intensity Field in TMC-1C*

The ACFs of the turbulent components of the total intensities of ^{13}CO and $C^{18}O$ are shown in Figures 5*d*, 5*e*, and 5*f*. The ACF of ^{13}CO in the 4′ × 4′ area does not show any correlation lengths, and the ACF of $C^{18}O$ in the same area shows a length of ~0.04 pc. For the core component mainly contributing to the ACF of the total intensity, the ^{13}CO line is emitted mainly from the surface of the cloud and traces the fluctuation of the surface temperature. On the other hand, the $C^{18}O$ line is approximately emitted from all over the line of sight and traces internal structures of the cloud. Therefore the correlation length of 0.04 pc probably reflects a typical size of clumps in the cloud. In Figures 3*c* and 4*c* the central peak or the ridge probably corresponds to the 0.04 pc scale. If there exists a clump with the size of 0.04 pc, then its mass is estimated to be ~0.1 $M_\odot$ from the total intensity of $C^{18}O$. Since the mass is smaller than the corresponding Jeans mass of ~1 $M_\odot$, the clumpy structure seen in TMC-1C is probably produced by the turbulence, and the fragmentation process due to the self-gravity does not dominate the turbulence. The CCS observations by Yamamoto et al. (1993) revealed two peaks having the size of ≈0.04 pc in a larger elongated clump with a size of 0.1 pc × 0.3 pc. The southeast peak seen in the clump corresponds to the central peak in Figures 3*c* and 4*c*. In the 8′ × 8′ area the ACF of ^{13}CO shows a correlation length of 0.05 pc. Since the ^{13}CO emission is optically thick for the core component, this scale does not correspond to the size of clumps but probably correspond to the scale seen in the fluctuation of the surface temperature of the cloud. In Figure 9*b* we fitted two models to the two-dimensional ACF of the $C^{18}O$ intensity: One is the model that the three-dimensional correlation function $B(r)$ in equation (A5) behaves as $\exp[-(r/l_c)^2]$, and the other is that the function behaves as $\exp[-(r/l_c)]$. The fitting is not good, although better fitting was done for the exponential type. Two kinds of slopes are required to improve the fitting, which is the same as in the velocity case. The fitted value of $l_c = 0.02$ pc for the exponential case is just the half of the apparent value of 0.04 pc in Figure 5*f*, as Kleiner & Dickman (1985) pointed out.

When a molecular line is optically thin, the total intensity of the line is represented by the line-of-sight integration of the product of the excitation temperature T_{ex} and absorption coefficient κ of the emitting gas. Therefore the ACF of the turbulent intensity field of $C^{18}O$ in Figure 5*f* is related to the scalar field of the product $T_{ex}\,\kappa$ of the turbulence. Since κ is roughly proportional to both the mass density ρ and the inverse square of the gas temperature, T^{-2}, the total intensity reflects the ratio of the gas density to temperature assuming $T \approx T_{ex}$. If the variation of T over clouds is smaller than that of ρ, then the total intensity directly reflects the integration of ρ along the line of sight. Only in such situations can we get some information of the density field of the turbulence from the variation of the total intensity over the cloud surface. In real molecular clouds, however, the variation of T over the the clouds is not negligible, and it is difficult to analyze the density field separately from the temperature field. On the contrary, the variations of ρ and T affect the calculations of the centroid velocities only to the first order, as pointed out by Dickman & Kleiner (1985), and we can analyze the velocity field without considering the variations of the gas density and temperature.

It is expected that the density field is connected with the velocity field through hydrodynamic equations including self-gravity, because molecular clouds are generally compressible. We calculate cross correlations between the velocity and intensity fields (Fig. 10). The cross correlations are normalized by the product of the two standard deviations in the velocity and intensity fields. For the velocity field both the ^{13}CO and $C^{18}O$ data are used, and for the intensity field only the $C^{18}O$ data are used. Although the cross correlations increase from negative values to positive values with increasing the lag, as expected from Figure 4, any significant correlations are not found. This fact may suggest that the compressibility is not dominant in the turbulence seen in TMC-1C, or that the intensity field does not correctly reflect the density field, owing to the variation of T along the line of sight, even if the physical link between the density and velocity fields is strong.

4.3. *The Power Spectrum of the Turbulent Velocity Field in TMC-1C*

It is shown that the estimated power spectra of the turbulent velocity and intensity fields do not show monotonic decrease like Kolmogorov's law, but decrease at the scales larger than ~0.05 pc and change into increase at the scales smaller than ~0.05 pc (Figs. 7*a* and 7*b*). At large scales, one peak appears at ~0.15 pc, probably because we subtracted the turbulent components with spatial scales larger than the size of the observed

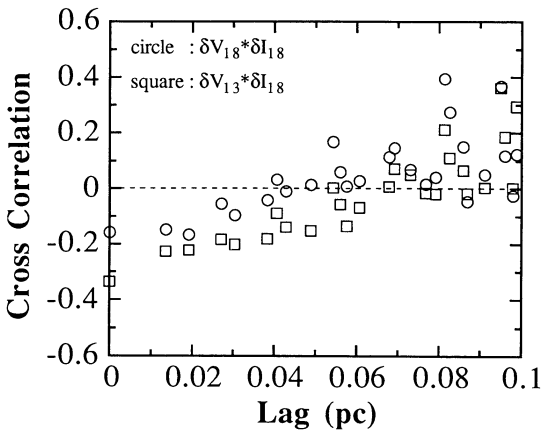

FIG. 10.—Cross-correlation between the turbulent velocity and intensity fields in the 4′ × 4′ area of TMC-1C. The correlations are normalized by the product of the two standard deviations of the turbulent velocity and intensity components. Circles show the cross correlation between the $C^{18}O$ velocity and $C^{18}O$ intensity, and squares show the cross correlation between the ^{13}CO velocity and $C^{18}O$ intensity.

area (0.16 pc) as a constant component. As stated previously, we found that the velocity ACF could not be well fitted by the Kolmogorov-type function. If the Kolmogorov-like turbulence is prevailing in TMC-1C, the profile of the spectrum in Figure 7*c* becomes a decreasing straight line whose slope is $-5/3$ in the range from 0.15 to 0.027 pc. In the Kolmogorov's picture, the energy of the turbulence that is input at the largest scale is cascaded down into smaller scales owing to the viscosity of the gas, and finally dissipates at the smallest scale, where new stars are formed. In real molecular clouds, however, it is difficult to suppose such a simple process, because compressibility and shock waves are prevailing at all spatial scales owing to the supersonic motions of the gas, and because the self-gravity of the clouds connects rotational motions to radial motions. Therefore, it is not surprising that Kolmogorov's law does not hold in TMC-1C, and we can expect more complicated spectra of the turbulence in TMC-1C, as Figure 7 shows.

Our estimated power spectrum of the velocity field can be shown to be equivalent to *the lateral three-dimensional spectrum F_{NN} of turbulence* after the correction for the beam pattern of a radio telescope, as shown by equation (B10). Note that the turbulence is assumed to be homogeneous and isotropic. The true power spectrum of the turbulence is defined in the three-dimensional cloud, and is changed in some degree into the two-dimensional spectrum $F_2(\boldsymbol{k}_2)$ owing to the integration along the line of sight. Therefore, we should know the three-dimensional spectrum $F_{zz}(\boldsymbol{k})$ that is Fourier-transformed from the three-dimensional correlation function $B_{zz}(\boldsymbol{r})$, instead of the two-dimensional spectrum $F_2(\boldsymbol{k}_2)$ transformed from the two-dimensional correlation function $B_2(\boldsymbol{r}_2)$. The relation between the two correlation functions $B_2(\boldsymbol{r}_2)$ and $B_{zz}(\boldsymbol{r})$ is expressed by equation (B3): The larger the distance from the cloud surface becomes, the more the information about the correlation function $B_{zz}(\boldsymbol{r})$ is lost, and it seems very difficult to estimate $F_{zz}(\boldsymbol{k})$ itself from $F_2(\boldsymbol{k}_2)$. However, we can obtain the lateral part F_{NN} of $F_{zz}(\boldsymbol{k})$ (see eq. [B9]), although the remaining longitudinal part F_{LL} cannot be estimated from our two-dimensional observed data.

Using an extended spectrum $F_{NN}^{\rm ext}$ derived from our estimated spectrum F_{NN} of the turbulent velocity field, we try to reproduce a two-dimensional correlation function $B_{\rm ext}$, which is averaged along the line of sight. We use the following transformation:

$$B_{\rm ext}(r_2) = \frac{1}{L}\int_0^L B_{zz}(r_2, z)dz \approx \frac{1}{L}\int_{1/D}^{1/2d} 2\pi k F_{NN}^{\rm ext}(k) J_0(2\pi k r_2)dk\ , \tag{6}$$

where L is the cloud depth, D is the size of the analyzed area, d is the grid spacing, and J_0 is the zeroth-order Bessel function. In this calculation we consider that the peak at 0.15 pc in Figure 7*a* is mainly due to the subtraction of large-scale motions in TMC-1C: The spectrum $F_{NN}^{\rm ext}$ at the scales larger than 0.15 pc is extrapolated from the spectrum F_{NN} at the scales from 0.15 to 0.05 pc in Figure 7*a*, and $F_{NN}^{\rm ext}$ agrees with F_{NN} at the scales smaller than 0.15 pc. We succeeded in reproducing a steep slope at small lags ($\lesssim$0.02 pc) and a gentle one at large lags in the case of $D = 0.16$ pc, as shown in Figure 11. Because of the existence of these two slopes, we could not successfully fit the three analytic functions to the velocity ACF in Figure 9*a*. The qualitative agreement between $B_{\rm ext}$ and our estimated velocity ACF validates our spectral estimation by the MEM. Besides, we can qualitatively reproduce the linear relation shown in Figure 8 by changing D in equation (6). This fact validates our interpretation of the velocity power spectrum and suggests that the correlation length defined by the ACF is not directly connected with a true physical scale owing to the incompleteness of our definition of turbulence. The correlation length only reflects the functional form of the power spectrum of the turbulence whose small-wavenumber part is cut off owing to the finite size of the observed area. It is noted that the real correlation length of $\sim$0.1 pc found in the $\sim 1° \times 1°$ area by Kleiner & Dickman (1987) is shorter than the scale of 0.5 pc that is expected in the $\sim 1° \times 1°$ area according to the linear relation in Figure 8. The relation shows a scale of 0.1 pc in a 12′ × 12′ (0.49 × 0.49 pc) area. Therefore, it is suggested that the power spectrum has a real peak at the wavenumber of $\sim 1/(0.49$ pc), which produces the 0.1 pc correlation length. In a small area where all components of turbulence cannot be recognized, it is essential to obtain power spectra of turbulence rather than correlation lengths.

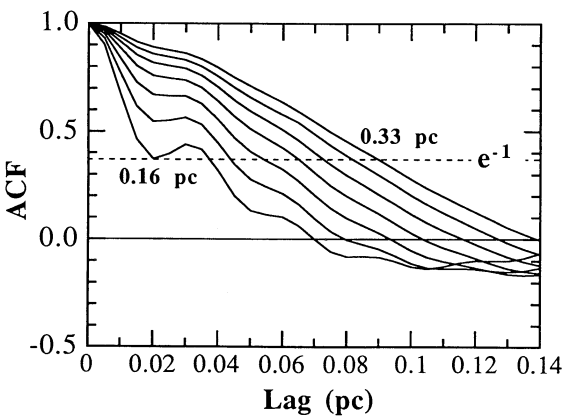

FIG. 11.—Autocorrelation functions reproduced from the model power spectrum of the turbulent velocity field of ^{13}CO in the 4′ × 4′ area. The model spectrum at the scales larger than 0.15 pc is extrapolated from the estimated power spectrum at the scales from 0.15 to 0.05 pc in Fig. 7*a*, and the model spectrum agrees with the estimated one in the range 0.15–0.027 pc. We changed the size of the analyzed area for the turbulence from 0.16 to 0.33 pc by an increment of 0.028 pc, corresponding to each profile from left to right. The level of e^{-1} is written by broken line.

At the scales where the turbulent motions prevail and the gas velocity is supersonic, clouds cannot gravitationally contract to form new stars inside them. At the scales where the turbulent motions decay and the gas velocity becomes subsonic, on the other hand, the clouds can contract by self-gravity, resulting in formation of new stars (Larson 1981; Myers 1983; Henriksen & Turner 1984). Stahler (1983) proposed that new stars are born in the clouds where thermal motions are dominant, from the analysis of the birthline of T Tauri stars. Therefore, it is important to answer why the energy of the lateral part of the turbulence per unit mass concentrates at the small scales of $\lesssim 0.03$ pc in TMC-1C. The similarity between the power spectra of the velocity and intensity fields may suggest that not only the energy per unit mass but also the energy per unit volume concentrates at the small scales, although we cannot directly estimate the energy per unit volume. At such small scales there may exist the energy input from new stars through some processes like stellar winds. In fact, one of the *IRAS* point sources is located at the south edge of TMC-1C (see Fig. 1), and is identified with the star, Haro 6-33, which has the bolometric luminosity of 0.37 $L_\odot$ (Myers et al. 1987). However, it is doubtful that the star is one of the driving sources for the turbulence, because the star is not located around the center of our observed areas and has no outflow. Another promising candidate for the driving sources of the turbulence is the self-gravity of the cloud. Léorat et al. (1990) simulated two-dimensional turbulence with low Mach numbers for the self-gravitating compressible fluid. Their density and velocity spectra do not show monotonic decrease. The density spectrum has a flat part at medium scales, and the velocity spectrum of the solenoidal part has a peak at a relatively large wavenumber, which may correspond to the increase at the scales smaller than 0.05 pc in our estimated velocity spectrum. Although the results of two-dimensional turbulence are not directly applicable to three-dimensional turbulence, it is possible that small cores in TMC-1C can have some energy due to gravitational contraction. First, some energy is injected into a giant molecular cloud with a spatial scale $l_{\rm in}$ by, for example, the galactic differential rotation. Next, some parts of the GMC contract into small fragments with the scale of $fl_{\rm in}$ ($0 < f < 1$). The factor f is evaluated to be $\lesssim 0.1$, according to the review by Scalo (1985). This process repeats until the appearance of the cores that directly contract into new stars. Unless these fragments in the hierarchical structure considerably lose their energy during the cloud lifetime owing to some processes like collision (Scalo & Pumphrey 1982), radiative cooling, and so on, the medium with the intermediate scales between $f^n l_{\rm in}$ and $f^{n+1} l_{\rm in}$ has less energy, and the profile of the velocity power spectrum shows an increase in the range of the wavenumber from $\sim 1/(f^n l_{\rm in})$ to $1/(f^{n+1} l_{\rm in})$, like our estimated spectrum in Figure 7.

On the other hand, the mass of a sphere with a radius of 0.03 pc is estimated to be $\sim 0.3\ M_\odot$ from the optically thin $C^{18}O$ data, which is smaller than the corresponding Jeans mass of $\sim 1\ M_\odot$. In the calculation of the Jeans mass we adopted the gas temperature of 10 K and the gas density of 10^4 cm^{-3}. If our estimation of the masses is true, the above comparison indicates that the self-gravity does not dominate in the small subcondensation TMC-1C. Therefore, the energy concentration at the small scales of ~ 0.03 pc must be attributed to the energy-transfer process of the turbulence itself, even if the turbulent motions presently seen in TMC-1C were generated by gravitational contraction at larger scales in the past.

For the case of the existence of energy input at small scales, the inverse energy cascade from small to large scales might occur. Levich & Tzvetkov (1985) explained mesoscale atmospheric phenomena seen on Earth by introducing the inverse cascade in three-dimensional turbulence. They showed that the energy injected into the atmosphere through deep convective clouds can be transformed into coherent motions of larger scales owing to the three-dimensional inverse cascade. Krishan (1991) applied this idea to the solar granulation, and Krishan & Sivaram (1991) applied it to the clustering of galaxies. The turbulence itself or both the turbulence and self-gravity probably provide the energy input at small scales in TMC-1C, which might trigger the inverse energy cascade, although we should quantitatively investigate whether the conditions for the inverse cascade hold in molecular clouds or not. A quantitative model of the compressible turbulence in self-gravitating clouds is proposed by Henriksen & Turner (1984). They considered the compressible, gravitationally driven, and angular momentum–limited turbulence, and derived the scaling laws including both the virial equilibrium and Larson's velocity-size relation (Larson 1981). This study strongly suggests the importance of the compressibility and self-gravity for the understanding of turbulence in molecular clouds. From an observational standpoint, it is very important to observe velocity and density structures of molecular clouds over large areas by Nyquist sampling, using radio telescopes with beams as small as possible. We have started making such laborious observations of the Taurus cloud by using the multibeam (four-beam) system equipped with the 45 m telescope of Nobeyama Radio Observatory in the winter of 1992.

5. SUMMARY

We have observed the turbulence seen in the $4' \times 4'$ and $8' \times 8'$ areas of the subcondensation TMC-1C in Heiles' cloud 2 by using the $^{13}CO(J = 1\text{–}0)$ and $C^{18}O(J = 1\text{–}0)$ lines with the spatial and velocity resolutions of 0.01 pc and 0.1 km s^{-1}, respectively. We have been able to extract the turbulent components whose wavelengths range from twice the grid spacing for our mapping to the size of our observed area. The turbulent velocity and intensity fields have been statistically analyzed by the autocorrelation and structure functions (ACFs and SFs), and the power spectra of the fields have been estimated from the ACFs. Our results are summarized as follows:

1. The estimation of both the optical depth and ACFs assures that the turbulent velocity field can be analyzed from the ^{13}CO wing component as well as from the $C^{18}O$ whole profile, and that the turbulent intensity field can be analyzed only from the $C^{18}O$ whole profile. For the calculation of the centroid velocity it is found that the contribution of the optically thin wing emission of ^{13}CO dominates that of the optically thick core emission.
2. The ACFs of the velocity fields of the ^{13}CO and $C^{18}O$ lines have similar correlation lengths of ~ 0.03 pc in the $4' \times 4'$ area, independent of their optical thickness. In the $8' \times 8'$ area the ACF of the ^{13}CO velocity field shows a correlation length of 0.07 pc. The ACF of the turbulent intensity field of the $C^{18}O$ line has a correlation length of 0.04 pc in the $4' \times 4'$ area.
3. The behaviors of the SFs agree well with those of the ACFs at the lags smaller than ~ 0.1 pc.
4. It is found that the correlation length defined by the ACF continuously increases with increasing the size of the analyzed area where the ACF is estimated, because we can analyze only

the turbulent components whose wavelengths range from twice the grid spacing for our mapping to the size of our observed area. Consequently, the correlation length defined by us in the areas smaller than the whole cloud does not directly correspond to a true physical scale in the subcondensation TMC-1C, because of the incompleteness of our definition of turbulence. In such small areas where all components of the turbulence cannot be recognized, we should rely not on the ACFs themselves, but on the power spectra obtained from the ACFs.

5. We have estimated the power spectra of the turbulent velocity and intensity fields from the ACFs. The velocity spectrum is shown to be equivalent to the lateral three-dimensional spectrum, if the homogeneous and isotropic turbulence is assumed. The spectra do not monotonically decrease in proportion to the wavenumber, and the velocity spectrum is inconsistent with Kolmogorov's 5/3 law. Although the spectra decrease at the wavenumbers smaller than 1/(0.05 pc), they come to increase at the wavenumbers from 1/(0.05 pc) to 1/(0.03 pc). This fact suggests that the energy of the lateral part of the turbulence per unit mass does not dissipate at the small scales of $\lesssim$0.03 pc but does concentrate.

6. The estimated velocity spectrum shows a peak at 0.15 pc, probably because the turbulent motions having the scales larger than $\sim$0.15 pc are removed as a constant component in our analysis. The apparent peak at 0.15 pc is expected to shift toward larger scales with enlarging the observed area up to $\sim$0.5 pc, and as a result the apparent correlation length defined by the velocity ACF for some components of the turbulence would proportionally lengthen up to $\sim$0.1 pc. The true scale of 0.1 pc found by Kleiner & Dickman (1987) strongly suggests the existence of a real peak at a wavenumber of $\sim$1/(0.5 pc) in the velocity spectrum.

The authors are grateful to the staff at the Nobeyama Radio Observatory (NRO) for operating the 45 m telescope and for their hospitality. They also thank R. Kawabe in NRO for useful comments and an anonymous referee for valuable suggestions. Y. K. acknowledges financial support from Itoh Science Foundation. The Nobeyama Radio Observatory, a branch of the National Astronomical Observatory, the Ministry of Education, Science, and Culture of Japan, is a cosmic radio observing facility open for outside users.

APPENDIX A

INFLUENCE OF THE BEAM PATTERN OF A RADIO TELESCOPE ON ACF

To examine the influence of the beam pattern of a radio telescope on autocorrelation functions (ACFs), we use the following approximate functional form of the beam pattern as

$$P(\theta) \approx \exp\left[-\ln 16\left(\frac{\theta}{\Theta}\right)^2\right] + 0.05\exp\left[-\ln 16\left(\frac{\theta-1.6\Theta}{0.5\Theta}\right)^2\right] + 1\times 10^{-3}\exp\left[-\ln 16\left(\frac{\theta}{\delta}\right)^2\right]. \quad \text{(A1)}$$

Here we consider Fraunhofer diffraction for a 13 dB tapered circular aperture, and we take account of the main Gaussian beam with the beam size (HPBW) of $\Theta \approx 17''$ (the first term), the second lobe appearing at the angular distance of 1.6Θ (the second term), and the error pattern with the angular width of $\delta \approx 10'$ corresponding to positional errors of the panels constituting a paraboloid of the telescope (the third term). The adopted values are appropriate to the Nobeyama 45 m telescope. The peak power of the second lobe is -13 dB, or 0.05, and for the error pattern the peak power is estimated from the beam efficiency ($\approx$0.4) and is found to be of the order of 10^{-3}.

When we observe a physical quantity a with a radio telescope having the beam pattern given by equation (A1), we will obtain an observed quantity A convolved with the beam pattern as

$$A(\boldsymbol{r}_2) = \int P(|\boldsymbol{r}_2 - \boldsymbol{r}'_2|)a(\boldsymbol{r}'_2)d\boldsymbol{r}'_2\,, \quad \text{(A2)}$$

where $\boldsymbol{r}_2$ and $\boldsymbol{r}'_2$ mean angular distances measured in the sky plane; the subscript 2 indicates quantities in the sky plane. For white-noise–like fields, we obtain an autocorrelation function $C(\boldsymbol{r}_2)$ as follows:

$$C(\boldsymbol{r}_2) = \frac{\int |A(\boldsymbol{k}_2)|^2 e^{i2\pi\boldsymbol{k}_2\cdot\boldsymbol{r}_2}\,d\boldsymbol{k}_2}{\int |A(\boldsymbol{k}_2)|^2\,d\boldsymbol{k}_2} = \exp\left(-\frac{\ln 4}{\Theta^2}\boldsymbol{r}_2^2\right), \quad \text{(A3)}$$

where $A(\boldsymbol{k}_2)$ means the Fourier transform of $A(\boldsymbol{r}_2)$. It is noted that the ACF produces a spurious correlation length of 0.85Θ for white noise. Besides, this result shows that minor lobes and error patterns do not have any influence on the ACF.

The two-dimensional ACFs are closely related to the three-dimensional ACFs, if we adopt the following assumptions: (1) A cloud is homogeneous and the excitation conditions of the observed lines are uniform; (2) the turbulent fields are isotropic; and (3) the observed lines are optically thin. The relation between the two- and three-dimensional ACFs was expressed by equation (III-33) in the paper by Kleiner & Dickman (1985). Since the influence of the beam pattern of a radio telescope was not taken into account in equation (III-33), we study the influence here.

The centroid velocity v_c, calculated from the velocity profile observed by a radio telescope at each grid point, is related with the radial velocity v_z of the cloud gas as follows:

$$v_c(\boldsymbol{r}_2) = \int \frac{\ln 16}{\pi\Theta^2}\exp\left[-\frac{\ln 16}{\Theta^2}(\boldsymbol{r}_2 - \boldsymbol{r}'_2)^2\right]\frac{1}{L}\int_0^L v_z(\boldsymbol{r}'_2, z)dz\,d\boldsymbol{r}'_2\,, \quad \text{(A4)}$$

where L is the depth of a cloud and z is measured from the cloud surface along the line of sight. In this relation we took account of only the main beam of a telescope, according to the above result (see eq. [A3]). Using equation (A4), we can extend equation (III-33) by Kleiner & Dickman (1985) in the case that observed data are convolved with the Gaussian beam of a radio telescope as

$$C(\boldsymbol{r}_2) = \frac{\langle \delta v_c(\boldsymbol{x}_2)\delta v_c(\boldsymbol{x}_2+\boldsymbol{r}_2)\rangle}{\langle \delta v_c(\boldsymbol{x}_2)\delta v_c(\boldsymbol{x}_2)\rangle} = \exp\left(-\ln 4\,\frac{r_2^2}{\Theta^2}\right)\frac{\int_0^\infty du\,u\exp(-\ln 4\cdot u^2)\cdot I_0[\ln 16(r_2/\Theta)u]\int_0^1 dx(1-x)\cdot B(\sqrt{\Theta^2u^2+L^2x^2})}{\int_0^\infty du\,u\cdot\exp(-\ln 4u^2)\int_0^1 dx(1-x)\cdot B(\sqrt{\Theta^2u^2+L^2x^2})}, \tag{A5}$$

where $C(\boldsymbol{r}_2)$ is the two-dimensional ACF, δv_c is the turbulent component of v_c, r_2 is the magnitude of the lag vector, I_0 is the zeroth order modified Bessel function of the first kind, and $B(r)$ is the three-dimensional correlation function. Here angle brackets denote an ensemble average. If we take $B(r) = \exp[-(r/l_c)^2]$ with a correlation length of l_c, for example, the two-dimensional ACF takes a simple functional form as

$$C(r_2) = \exp\left[-\frac{r_2^2}{l_c^2+(\Theta^2/\ln 4)}\right], \tag{A6}$$

and the apparent correlation length becomes $\sqrt{l_c^2+(\Theta^2/\ln 4)}$.

APPENDIX B

INTERPRETATION OF THE POWER SPECTRUM ESTIMATED FROM OBSERVED VELOCITY FIELD

From two-dimensional observed data, we can estimate the lateral three-dimensional spectrum of the turbulence in molecular clouds. For the homogeneous and isotropic turbulence the component of the correlation tensor, B_{zz} is defined by the turbulent component of the radial velocity, δv_z as follows:

$$B_{zz}(\boldsymbol{r}) \equiv \langle \delta v_z(\boldsymbol{x})\delta v_z(\boldsymbol{x}+\boldsymbol{r})\rangle = [B_{LL}(\sqrt{r_2^2+z^2}) - B_{NN}(\sqrt{r_2^2+z^2})]\frac{z^2}{r_2^2+z^2} + B_{NN}(\sqrt{r_2^2+z^2}), \tag{B1}$$

where $\boldsymbol{r} = (\boldsymbol{r}_2, z)$ is a lag vector, and B_{LL} and B_{NN} are longitudinal and lateral correlation functions (Monin & Yaglom 1977). Here angle brackets denote an ensemble average, $\boldsymbol{r}_2$ is in the sky plane, and z is measured from the cloud surface along the line of sight; the subscript 2 indicates quantities measured in the sky plane. For a solenoidal isotripic field, for example, B_{LL} and B_{NN} are not independent of each other, and B_{NN} is expressed by B_{LL} as

$$B_{NN}(r) = B_{LL}(r) + \frac{r}{2}\frac{d}{dr}B_{LL}(r). \tag{B2}$$

The two-dimensional correlation function $B_2(\boldsymbol{r}_2)$, which is calculated from the fluctuating component of the centroid velocities averaged along the line of sight, is related with $B_{zz}(\boldsymbol{r})$ as follows:

$$B_2(\boldsymbol{r}_2) = \frac{2}{L}\int_0^L\left(1-\frac{z}{L}\right)B_{zz}(\boldsymbol{r}_2, z)dz = \frac{2}{L}\int_0^L\left(1-\frac{z}{L}\right)B_{zz}(\sqrt{r_2^2+z^2})dz, \tag{B3}$$

where L is the depth of a cloud. The correlation function directly derived from the turbulent component of the observed velocity field (see eq. [A4]), $B_{\rm obs}(\boldsymbol{r}_2)$ is expressed as a convolution of the beam pattern and the correlation function $B_2(\boldsymbol{r}_2)$:

$$B_{\rm obs}(\boldsymbol{r}_2) = \frac{\ln 4}{\pi\Theta^2}\int\exp\left[-\frac{\ln 4}{\Theta^2}(\boldsymbol{r}_2+\boldsymbol{s}_2)^2\right]B_2(\boldsymbol{s}_2)d\boldsymbol{s}_2, \tag{B4}$$

where Θ is the beam size (HPBW) of a radio telescope. Since power spectra are converted from the correlation functions by the Fourier transformation, we have

$$F_{\rm obs}(\boldsymbol{k}_2) = \exp\left(-\frac{\pi^2\Theta^2}{\ln 4}\boldsymbol{k}_2^2\right)F_2(-\boldsymbol{k}_2), \tag{B5}$$

where $F_{\rm obs}(\boldsymbol{k}_2)$ and $F_2(\boldsymbol{k}_2)$ are the power spectra converted from $B_{\rm obs}(\boldsymbol{r}_2)$ and $B_2(\boldsymbol{r}_2)$ by the Fourier transformation, respectively, and $\boldsymbol{k}_2$ means the wavenumber vector in the sky plane. Therefore, the two-dimensional power spectrum estimated from the observed data, $F_{\rm obs}(\boldsymbol{k}_2)$ is related to B_{zz} as follows:

$$F_{\rm obs}(\boldsymbol{k}_2) = \exp\left(-\frac{\pi^2\Theta^2}{\ln 4}\boldsymbol{k}_2^2\right)\int d\boldsymbol{s}_2\frac{2}{L}\int_0^L\left(1-\frac{z}{L}\right)B_{zz}(\boldsymbol{s}_2, z)dz\,e^{+i2\pi\boldsymbol{k}_2\cdot\boldsymbol{s}_2}. \tag{B6}$$

Since the component of the spectral tensor, F_{zz} is defined by B_{zz} as follows:

$$F_{zz}(\boldsymbol{k}_2, k_z) = \int B_{zz}(\boldsymbol{r}_2, z)e^{-i2\pi\boldsymbol{k}_2\cdot\boldsymbol{r}_2}e^{-i2\pi k_z z}d\boldsymbol{r}_2\,dz, \tag{B7}$$

the component F_{zz} can be approximately connected with the spectrum $F_{obs}(\boldsymbol{k}_2)$ as

$$F_{zz}(\boldsymbol{k}_2, 0) = \int B_{zz}(\boldsymbol{r}_2, z) e^{-i2\pi \boldsymbol{k}_2 \cdot \boldsymbol{r}_2} d\boldsymbol{r}_2 \, dz = \int d\boldsymbol{r}_2 \left[\int B_{zz}(\boldsymbol{r}_2, z) \, dz \right] e^{-i2\pi \boldsymbol{k}_2 \cdot \boldsymbol{r}_2} \approx \frac{L}{2} \exp\left(\frac{\pi^2 \Theta^2}{\ln 4} \boldsymbol{k}_2^2 \right) F_{obs}(-\boldsymbol{k}_2) \, . \tag{B8}$$

Here we neglect the term $(1 - z/L)$. If B_{zz} approaches zero at lags much smaller than L, the term $(1 - z/L)$ can be regarded as unity. Like equation (B1), the component F_{zz} is expressed as

$$F_{zz}(\boldsymbol{k}_2, k_z) = [F_{LL}(\sqrt{\boldsymbol{k}_2^2 + k_z^2}) - F_{NN}(\sqrt{\boldsymbol{k}_2^2 + k_z^2})] \frac{k_z^2}{\boldsymbol{k}_2^2 + k_z^2} + F_{NN}(\sqrt{\boldsymbol{k}_2^2 + k_z^2}) \, , \tag{B9}$$

where the functions F_{LL} and F_{NN} are called longitudinal and lateral three-dimensional spectra. Consequently the lateral three-dimensional spectrum F_{NN} can be evaluated from the two-dimensional power spectrum corrected for the beam pattern as

$$F_{NN}(|\boldsymbol{k}_2|) = F_{zz}(\boldsymbol{k}_2, 0) \approx \frac{L}{2} \exp\left(\frac{\pi^2 \Theta^2}{\ln 4} \boldsymbol{k}_2^2 \right) F_{obs}(-\boldsymbol{k}_2) \, . \tag{B10}$$

The spectrum integrated with respect to the angular direction of the wavenumber vector, $E(k)$, is written as

$$E(k) = 2\pi k^2 [2F_{NN}(k) + F_{LL}(k)] \, . \tag{B11}$$

From our two-dimensional data, we cannot estimate the longitudinal three-dimensional spectrum F_{LL}. In the solenoidal isotropic case, F_{LL} vanishes, and $E(k)$ can be estimated only from F_{NN}.

REFERENCES

Cohen, M., & Kuhi, L. V. 1979, ApJS, 41, 743
Dickman, R. L., & Kleiner, S. C. 1985, ApJ, 295, 479
Elias, J. H. 1978, ApJ, 224, 857
Falgarone, E. 1989, in IAU Colloq. 120, Structure and Dynamics of the Interstellar Medium, ed. G. Tenorio-Tagle, M. Moles, & J. Melnick (Berlin: Springer-Verlag), 68
Falgarone, E., & Phillips, T. G. 1990, ApJ, 359, 344
Henriksen, R. N., & Turner, B. E. 1984, ApJ, 287, 200
Houlahan, P., & Scalo, J. 1990, ApJS, 72, 133
Kleiner, S. C., & Dickman, R. L. 1984, ApJ, 286, 255
———. 1985, ApJ, 295, 466
———. 1987, ApJ, 312, 837
Krishan, V. 1991, MNRAS, 250, 50
Krishan, V., & Sivaram, C. 1991, MNRAS, 250, 157
Kutner, M. L., & Ulich, B. L. 1981, ApJ, 250, 341
Larson, R. B. 1981, MNRAS, 194, 809
Léorat, J., Passot, T., & Pouquet, A. 1990, MNRAS, 243, 293
Levich, E., & Tzvetkov, E. 1985, Phys. Rep., 128, 1
Monin, A. S., & Yaglom, A. M. 1977, Statistical Fluid Mechanics: Mechanics of Turbulence, Vol. 2 (Cambridge, Mass: The MIT Press)
Myers, P. C. 1983, ApJ, 270, 105
Myers, P. C., Fuller, G. A., Mathieu, R. D., Beichman, C. A., Benson, P. J., Schild, R. E., & Emerson, J. P. 1987, ApJ, 319, 340
O'Dell, C. R., & Castañeda, H. O. 1987, ApJ, 317, 686
Ong, C. 1971, in Long Period Array Processing Report 1 (Texas Instruments, Inc.)
Passot, T., Pouquet, A., & Woodward, P. 1988, A&A, 197, 228
Scalo, J. M. 1984, ApJ, 277, 556
———. 1985, in Protostars and Planets II, ed. D. C. Black & M. S. Matthews (Tucson: The University of Arizona Press), 201
Scalo, J. M., & Pumphrey, W. A. 1982, ApJ, 258, L29
Schloerb, F. P., & Snell, R. L. 1984, ApJ, 283, 129
Snell, R. L., Scoville, N. Z., Sanders, D. B., & Erickson, N. R. 1984, ApJ, 284, 176
Stahler, S. W. 1983, ApJ, 274, 822
Woods, J. W. 1976, IEEE Trans. Inform. Theory, IT-22, 552
Yamamoto, S., et al. 1993, in preparation